Energy-resolved attosecond interferometric photoemission from Ag(111) and Au(111) surfaces

M. J. Ambrosio and U. Thumm

Physics Department, Kansas State University, Manhattan, Kansas 66506, USA

Photoelectron emission from solid surfaces induced by attosecond pulse trains into the electric field of delayed phase-coherent infrared (IR) pulses allows the surface-specific observation of energy-resolved electronic phase accumulations and photoemission delays. We quantum-mechanically modeled interferometric photoemission spectra from the (111) surfaces of Au and Ag, including background contributions from secondary electrons and direct emission by the IR pulse, and adjusted parameters of our model to energy-resolved photoelectron spectra recently measured at a synchrotron light source by Roth *et al.* [J. Electron Spectrosc. **224**, 84 (2018)]. Our calculated spectra and photoelectron phase shifts are in fair agreement with the experimental data of Locher *et al.* [Optica **2**, 405 (2015)]. Our model's not reproducing the measured energy-dependent oscillations of the Ag(111) photoemission phases may be interpreted as evidence for subtle band-structure effects on the final-state photoelectron-surface interaction not accounted for in our simulation.

I. INTRODUCTION

Complementing established energy-resolved photoelectron spectroscopy [1], time-resolved spectroscopic methods based on photoemission by ultrashort extreme-ultraviolet (XUV) pulses into the electric field of an assisting time-delayed phase-coherent infrared (IR) laser pulse have been developed during the past two decades [2–4] and applied to probe the light-induced electronic dynamics in atoms [5–10], molecules [11], and solids [12–20] with atomic time resolution, i.e., at the intrinsic attosecond time scale of the electronic motion in matter (1 as = 10^{-18} s, 1 a.u. = 1 atomic time unit = 24 as). Such time-resolved photoemission experiments are carried out in two distinct ways, photoemitting electrons with either isolated attosecond XUV pulses (IAPs) or attosecond XUV pulse trains (APTs). Both types of experiments record photoelectron spectra as functions of the photoelectron kinetic energy and XUV-IR pulse delay. While streaked photoemission spectroscopy employs IAPs and reveals temporal information about the photoemission process in terms of delay-dependent photoelectron energy shifts [3,5,6,14,20], the use of APTs in RABBITT (reconstruction of attosecond beating by interference of two-photon transitions) experiments provides sub-IR-cycle time resolution by detecting delay-dependent changes of the photoelectron yield [7,15,18,21]. Both photoelectron-energy and yield oscillations follow in time the carrier-field oscillations of the IR pulse with characteristic photoelectron-energy-dependent phase shifts. The yield oscillations in RABBITT spectra are due to sideband interferences of the IR-pulse-assisted XUV photoemission [22,23].

The ionizing XUV IAPs and APTs in these two spectroscopic methods, streaked and RABBITT time-resolved photoelectron-emission spectroscopy, respectively, are provided by splitting the primary IR laser pulse into the assisting IR pulse and a component that generates high-order harmonics (HHs) upon irradiation of a gas-filled cell. The resulting HHs can be spectrally filtered and combined to produce IAPs and APTs that are phase coherent relative to the assisting IR pulse.

By sending one of the split IR pulses through a delay stage, the relative delay of the XUV and assisting IR pulse can be scanned with subfemtosecond precision. APTs obtained by HH generation are characterized by their spectral range and amplitude and the phases of their individual HH constituents. The HH phases of the APT thus contribute to the observable energy-dependent phases of the yield oscillation in RABBITT spectra. They are usually unknown, but can be eliminated by either simultaneously *in situ* recording a (well-understood) RABBITT spectrum from a reference target [15,16,19,23] or by simultaneously determining RABBITT phase differences in the photoemission from energetically discernible initial states of the same target [17,18].

Locher *et al.* [15] recently measured RABBITT spectra from Ag(111) and Au(111) and deduced RABBITT phases for these surfaces by eliminating the HH phases of the APT with reference to spectra recorded *in situ* from an argon gas target. Furthermore, by subtracting calculated photoemission phases for argon [22] Locher *et al.* obtained the absolute RABBITT scattering phases for the two surfaces. These energy-dependent phases characterize the phase accumulation during the entire surface-photoemission process. They include contributions from the initial photoelectron excitation by the APT in the solid, photoelectron propagation to the surface, the subsequent side-band-producing interaction of the photoelectron with the IR pulse, and Fresnel reflection of the IR pulse at the surface [23,24]. The assessment of the relative importance of these phase increments and their underlying elementary interactions of the photoelectron with the solid, APT, and IR pulse is impossible based solely on the measured spectra and requires theoretical modeling.

In this work we employ a quantum-mechanical model in order to calculate RABBITT spectra and phases from Ag(111) and Au(111) surfaces, adjusting the pulse incidence and electron-emission geometry, as well as APT and IR pulse parameters to the experiment of Locher *et al.* (Fig. 1). In this geometry both pulses are *p* polarized and incident under an angle
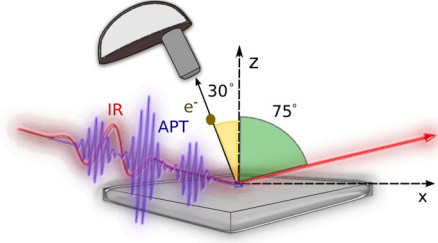
FIG. 1. Schematic of interferometric photoemission spectroscopy applied to atomically flat Ag(111) and Au(111) surfaces in this work. The mutually delayed ionizing XUV attosecond pulse train and assisting IR laser pulse are linearly p polarized and incident under an angle of 75° relative to the surface normal. Photoelectrons are detected with a hemispherical electron analyzer, the acceptance cone of which is centered 30° from the positive z axis in the IR-pulse-reflection (xz) plane toward the negative x axis, with an acceptance angle of 30°.

of 75° relative to the surface normal, while photoelectrons are detected with a hemispherical electron analyzer. We represent the initial valence band and final photoelectron states within a tight-binding model [25] and in terms of modified semiclassical Volkov final states [26,27], respectively, and adjust open parameters in our simulation to obtain the best overall visual agreement with the experimental RABBITT spectra. Our model includes a phenomenological simulation of background contributions to the photoemission spectra from secondary electrons generated by the APT and from direct photoemission by the IR pulse. We adjusted this delay-independent photoemission background to energy-resolved XUV photoelectron spectra for Ag(111) and Au(111) that were recently measured with synchrotron radiation by Roth *et al.* [28]. Our model calculations are in fair agreement with the measured RABBITT spectra and RABBITT phases of Locher *et al.* [15]. However, our model does not reproduce their observed energy-dependent oscillation of the Ag(111) RABBITT phases. Since we employ photoelectron final states that do not include details of the target band structure, the absence of RABBITT phase oscillations in our simulation is consistent with recent experimental evidence of subtle band-structure effects influencing final photoelectron states [15,17,18]. Throughout this work we use atomic units unless stated otherwise and define the energy-scale zero as the ionization threshold.

II. THEORY

The photoelectron yield for a given photoelectron final energy $\varepsilon_f = k_f^2/2$ and time delay τ between the APT and assisting laser pulse is given by the incoherent sum over all occupied initial conduction-band states of the target surface,

$$P_0(\mathbf{k}_f, \tau) = \sum_{|\mathbf{k}_i| < k_F} \left| T_{\mathbf{k}_f, \mathbf{k}_i}(\tau) \right|^2. \tag{1}$$

We calculate the transition amplitude between the tight-binding initial state $\Psi_{\mathbf{k}_i}^i$ and a modified Volkov final state $\Psi_{\mathbf{k}_f}^f$,

$$T_{\mathbf{k}_f, \mathbf{k}_i}(\tau) \propto \int_{-\infty}^{\infty} dt \langle \Psi_{\mathbf{k}_f}^f(\mathbf{r}, t, \tau) | \mathbf{A}_{\mathrm{XUV}}(z, t) \cdot \nabla | \Psi_{\mathbf{k}_i}^i(\mathbf{r}, t) \rangle. \tag{2}$$
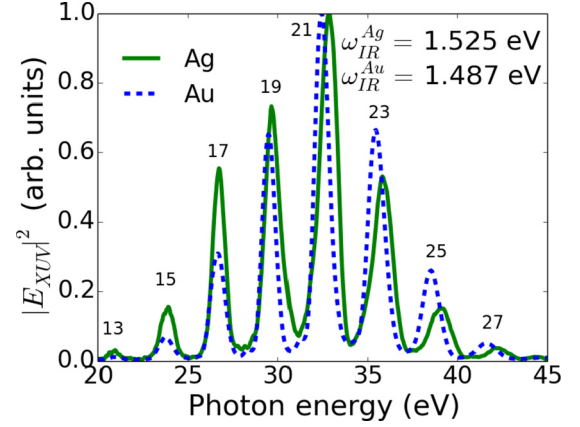

FIG. 2. Electric-field intensities of the attosecond pulse trains employed in interferometric photoemission from Ag(111) and Au(111) surfaces in Ref. [15]. Adapted from Ref. [29]. Individual higher-order-harmonics peaks are labeled by their harmonic orders.

$\mathbf{A}_{\mathrm{XUV}}(z, t)$ is the vector potential of the inhomogeneous APT. We represent the APT interaction with conduction electrons in the nondipole velocity gauge, thereby allowing for arbitrary electron emission directions. In compliance with typical XUV-APT intensities in RABBITT experiments [15,18], we assume in Eq. (2) that the XUV APT intensity is low enough for $\mathbf{A}_{\mathrm{XUV}}$ to be included perturbatively.

In accordance with the RABBITT experiment by Locher *et al.* [15], we assume the XUV APT to be composed of odd HHs 13 through 27, each with an energy width (full amplitude width at half maximum, FAWHM) of 1 eV, and match the corresponding spectral amplitudes to the experimental electric-field amplitudes $E_{\mathrm{XUV}}(z, t) = -dA_{\mathrm{XUV}}(z, t)/dt$ shown in Fig. 2 [29]. Due to the finite inelastic mean free path [30] at the energies of interest, the photoelectron escape depth is limited to a few lattice spacings, $a_s^{\mathrm{Ag}} = 4.43$ and $a_s^{\mathrm{Au}} = 4.45$ of Ag(111) and Au(111), respectively [31], and thus much smaller than the XUV skin depth (which is larger than 200 a.u. [32]). Accordingly we may assume that the APT propagates without being deflected by or attenuated inside the solid. In the prototypical experiment of Locher *et al.* [15], the detector electron acceptance angle was deliberately kept wide [29] in order to maximize the signal-to-noise ratio. We therefore assume an acceptance angle of 30°. The electron detector was centered at an angle of 30° off the surface normal on the incident side of the IR-pulse-reflection plane (Fig. 1).

In our numerical applications, we adopt the pulse incidence and electron-detection geometry, as well as the APT and IR-pulse parameters of Ref. [15]. Accordingly we assume an IR-pulse peak intensity of 3×10^{11} W/cm^2 and an IR-pulse width of 10 fs (FAWHM). We extract the IR-photon energies from Fig. 2. They amount to 1.525 and 1.487 eV for interferometric photoemission from the Ag and Au surface, respectively.

A. Initial state

We describe the initial valence-band states of the active electron by the translationally invariant wave functions

$$\Psi_{\mathbf{k}_i}^i(\mathbf{r}, t) = e^{i\mathbf{k}_{i,\parallel} \cdot \mathbf{r}_\parallel} \phi_{k_{i,z}}(z) e^{-iE_{\mathrm{bnd}}t}, \tag{3}$$

representing the electronic motion along the surface normal direction (z axis) as a linear combination of Hulthén generalized Sturmian functions (GSFs) [33–35] φ,

$$\phi_{k_{i,z}}(z) = \sum_j e^{ik_{iz}z_j}\varphi(E_{\text{TB}},\alpha,n,|z - z_j|). \qquad (4)$$

We define $z = 0$ at the surface layer of lattice points. The atomic orbitals φ are centered at the atomic layers z_j with the layer separations a_s^{Ag} and a_s^{Au} of Ag(111) and Au(111), respectively. We previously applied this tight-binding initial-state model to photoemission from the Cu(111) d band [25] in good agreement with experimental interferometric photoemission spectra [16].

The GSFs $\varphi(E_{\text{TB}},\alpha,n,u)$ model the active electron immersed in the screened Coulomb potential of an atomic core and are known analytically in terms of hypergeometric functions as solutions of a one-dimensional (1D) generalized potential-eigenvalue problem [25,33]. The adjustable energy E_{TB} determines the rate of exponential decrease of the electronic probability density with the distance $u = |z - z_j|$ from the atomic nucleus. In zero-bandwidth approximation, we set E_{bnd} equal to -10.36 and -11.33 eV for the Ag(111) and Au(111) surface, respectively. We obtained these values for E_{bnd} by linear extrapolation of the photoelectron energy $\varepsilon_f = \omega_{\text{XUV}}^{\text{HH/SB}} - E_{\text{bnd}}$ as a function of the HH and sideband (SB) energies, $\omega_{\text{XUV}}^{\text{HH}}$ and $\omega_{\text{XUV}}^{\text{SB}}$ to $\omega = 0$. These values are within the range of the d-band binding energies given in energy-resolved photoemission spectra in Refs. [36,37] and are used for all calculations discussed in this work. We further set $E_{\text{TB}} = E_{\text{bnd}}$.

The parameter α determines the distribution of wave-function nodes, while n specifies the number of nodes. Smaller values of α imply a higher density of nodes near the atomic nucleus [33]. We separately specified α and n for the two surfaces by fitting the energy-resolved spectra of Roth *et al.* [28], as will be detailed in Sec. III A below. A full 3D representation of the initial state, modeling photoemission from the d bands of Ag and Au, would require the initial orbitals to include the photoelectron angular-momentum component m along the surface normal in terms of the factor $e^{im\phi}$. However, for the assumed translational invariance in the surface (x,y plane), orbitals with nonzero m average to zero, and the only contributing ($l = 2$, $m = 0$) 3D orbitals have positive parity. Consistent with our assumption of translational invariance, we therefore select 1D atomic orbitals with positive parity by defining $\varphi(E_{\text{TB}},\alpha,n,u) \equiv \varphi(E_{\text{TB}},\alpha,n,-u)$ for $z < z_j$.

B. Final state

The final state incorporates the interaction of the photoelectron with the inhomogeneous, screened laser electric field and the surface. We model the final state by modifying the well-known Volkov wave function for an electron in a homogenous continuum-wave electric field [38] according to

$$\Psi_{\mathbf{k}_f}^f(\mathbf{r},t,\tau) \propto f_{\varepsilon_f,\theta_f}(z)e^{i\mathbf{k}_{f,\parallel}\cdot\mathbf{r}_\parallel}\psi_{k_{f,z}}(z)e^{i\phi_{\mathbf{k}_f}(z,t_d)}e^{-i\varepsilon_f t},$$
$$(5)$$

with $t_d = t - \tau$. The key elements of this heuristic generalization are (i) the damping factor $f_{\varepsilon_f,\theta_f}(z)$, (ii) the inclusion of a potential step of height U_0 at the surface, and (iii)

the generalization of the Volkov phase $\phi_{\mathbf{k}_f}$ describing the photoelectron interaction with the inhomogeneous, pulsed laser electric field [25,26]:

(i) The damping factor

$$f_{\varepsilon_f,\theta_f}(z) = \Theta(z) + e^{z/[2\lambda(\varepsilon_f)\cos(\theta_f)]}\Theta(-z) \qquad (6)$$

accounts for the loss of emission probability from deeper layers. $\Theta(z)$ designates the Heaviside step function with function values of 0 and 1 for $z < 0$ and $z \geq 0$, respectively. With the energy-dependent mean free path $\lambda(\varepsilon_f)$ we include the loss of electron yield due to scattering of the XUV-excited photoelectron before being emitted from the solid. For the numerical application in this work, we use the mean free path values given in Ref. [30].

(ii) With the step potential $-U_0\Theta(z_{\text{im}} - z)$ and the image-plane positions $z_{\text{im}} = 2.22$ and 2.12 a.u. for Ag(111) and Au(111), respectively [31], the z-dependent wave function $\psi_{k_{f,z}}$ accounts for the decrease of kinetic energy at the surface during photoelectron emission [25]. The step potential is also included in our semiclassical calculation of the Volkov phase factor $e^{i\phi_{\mathbf{k}_f}(z,t_d)}$ discussed in the following two paragraphs. U_0 is a free parameter of our final-state description. We adjust this parameter to match measured photoemission spectra (see Sec. III A below).

(iii-1) Fresnel reflection of the incident IR pulse at the metal optical surface $z = z_{\text{IR}}$ generates transmitted and specularly reflected electric fields. We calculate the transmitted and reflected IR electric fields by solving Fresnel's equations [23,39] based on the macroscopic, complex-valued dielectric function $\varepsilon(\omega_{\text{IR}})$ which was derived within a Lorentz-Drude model [40] and yields good agreement with the transmission and reflection measurements on thin Ag and Au films by Johnson and Christy [41]. Fresnel's equations, being macroscopic in nature, imply a discontinuity of the normal electric-field component at z_{IR}. Based on a time-dependent DFT calculation, an exponential-screening model and experimental data for Mg atomic layers adsorbed on W(100), Neppl *et al.* [14] estimated the IR skin depth for Mg surfaces to be of the order of one lattice spacing. At $\hbar\omega_{\text{IR}} = 1.5$ eV the extinction coefficients for Ag, Au, and Mg are of the same order of magnitude [32]. We therefore adopt comparable, but adjustable, values for z_{IR} for Ag and Au, generously limiting z_{IR} to lie between the second lattice plane and half a lattice constant outside the top layer of atomic nuclei, assuming full screening of the IR electric field for $z < z_{\text{IR}}$.

(iii-2) We account for the photoelectron transport to the surface by calculating the IR-pulse vector potential

$$\mathbf{A}_{\text{IR}}(z_j,t_d) = \int_{t_{\text{surf}}}^\infty dt'\mathbf{E}_{\text{IR}}(\tilde{z}(t'),t_d') \qquad (7)$$

in the generalized Volkov phase

$$\phi_{\mathbf{k}_f}(z_j,t_d) = \mathbf{k}_f \cdot \int_t^\infty dt'\mathbf{A}_{\text{IR}}(z_j,t_d') \qquad (8)$$

along classical ballistic photoelectron trajectories $\tilde{z}(t)$ [26,27]. Consistent with the IR intensities applied in typical RABBITT experiments [15,18], we neglected the ponderomotive term ($\sim\mathbf{A}_{\text{IR}}^2$) in $\phi_{\mathbf{k}_f}$. These trajectories describe photoelectron propagation inside the solid. They start at the release time t from each atomic plane location z_j and reach the onset of dielectric

screening of the incident IR pulse $z_{\rm IR}$ at time $t_{\rm surf}$. At $z_{\rm im}$ the trajectories traverse the potential step of height U_0.

For Fresnel reflection at a precisely defined effective optical surface, the time integrations in Eqs. (7) and (8) can be performed analytically, and only the time integration in the transition amplitude (1) needs to be carried out numerically.

C. Secondary electrons and IR background

The measured photoelectron yields in Ref. [15] include delay-independent background contributions from secondary electrons generated during the XUV photoemission and electrons generated by above-threshold ionization (ATI) by the IR pulse. We account for the secondary-electron background within a phenomenological model and include the ATI background by fitting experimental data in Ref. [15].

We include the background of ATI electrons

$$P_{\rm IR}^{\rm bgr}(\varepsilon_f) = C_1 e^{-\varepsilon_f/\gamma_{\rm IR}} + C_2 \qquad (9)$$

by adjusting the exponential-decay parameter $\gamma_{\rm IR}$ and the constants C_1 and C_2 to reproduce the experimental data for Ag(111) in Fig. 1(d) of Ref. [15] over the ε_f interval [10, 30] eV. This yields $\gamma_{\rm IR} = 0.25231$, $C_1 = 3.41716$, and $C_2 = 0.03298$. Due to the lack of corresponding experimental ATI-background data for Au(111), we also apply these values in our calculations for Au(111) surfaces. We note, however, that this inconsistency is largely corrected by our target-specific scaling of the IR background [see scaling factor $\mathcal{B}_{\rm IR}$ in Eq. (13) and Sec. III B below].

We model the secondary-electron background based on the decrease of the photoelectron yield at a given photoelectron energy due to elastic scattering of the to-be-emitted XUV-excited electron off other valence-band electrons. Owing to the large mass difference, electron scattering with the nuclei does not noticeably reduce the photoelectron kinetic energy and can be neglected. We thus allow a fraction of the XUV-excited electrons to scatter and lose energy inside the substrate before reaching the surface-vacuum interface. We further assume that randomly scattered photoexcited electrons have lost all phase information of the exciting APT and therefore do not include them in our simulation of the delay-dependent interferometric photoemission yield. We further assume stationary target electrons and represent their interaction with the photoexcited projectile electrons in terms of the screened Coulomb-interaction potential $\propto e^{-r/\alpha_Y}/r$, where r is the interelectronic distance. The screening length α_Y accounts for the shielding of the electronic Coulomb interaction by the background charge of the solid and is comparable to the Thomas-Fermi screening lengths for metals [42]. Starting with the first Born approximation for the electron-electron scattering cross section, differential in the scattering angle $\theta_{\rm c.m.}$ in the center-of-mass (c.m.) frame of reference of the colliding electrons $d\sigma/d\Omega_{\rm c.m.}(\theta_{\rm c.m.}) \propto [\alpha_Y^{-2} + q^2]^{-2}$ [43], we find the scattering angle $\theta_L = \theta_{\rm c.m.}/2$, cross section $d\sigma/d\Omega_L(\theta_L) = 4\cos\theta_L \, d\sigma/d\Omega_{\rm c.m.}(\theta_{\rm c.m.})$, and energy loss of the scattering electron in the laboratory (L) frame of reference [44].

In the laboratory frame, the excited electron loses some of its incident energy $\varepsilon_f^{\rm in}$ to the substrate electron. Due to their equal mass, the scattered and recoiling electrons leave the collision in perpendicular directions, such that only one of them can enter the detection cone. $\varepsilon_f^{\rm in}$ and the scattered (final) energy ε_f of the photoelectron are related to the scattering angle as $\cos\theta_L = \sqrt{\varepsilon_f/\varepsilon_f^{\rm in}}$. From the cross section, which is a measure for the probability of an electron with energy $\varepsilon_f^{\rm in}$ to be slowed to an energy ε_f, we derive the integral kernel

$$K(\varepsilon_f, \varepsilon^{\rm in}) = N(\varepsilon_f) \frac{\sqrt{\varepsilon_f/\varepsilon_f^{\rm in}}}{\left[\alpha_Y^{-2} + 2(\varepsilon_f^{\rm in} - \varepsilon_f)\right]^2} \qquad (10)$$

for the shift of photoelectron yield from a small energy bin centered at $\varepsilon_f^{\rm in}$ to a small bin around the lower energy ε_f. The delay-independent secondary-electron yield is now given by

$$P_{\rm XUV}^{\rm bgr}(\varepsilon_f) = \int_{\varepsilon_f}^{\varepsilon_{\rm max}} d\varepsilon_f^{\rm in} K(\varepsilon_f, \varepsilon_f^{\rm in}) P_{\rm XUV}(\varepsilon_f^{\rm in}). \qquad (11)$$

$P_{\rm XUV}$ is the photoelectron yield generated by the APT, calculated according to Eq. (1), but without including the assisting IR laser field. The upper integration limit $\varepsilon_{\rm max}$ needs to be larger than the kinetic energy of direct photoelectrons that are released by the highest HH in the APT. With the numerically calculated normalization factor $N(\varepsilon_f)$ we energy normalize $P_{\rm XUV}^{\rm bgr}$ to the net APT-only yield $P_{\rm XUV}$ (see Sec. III B below). In order to compare calculated and measured RABBITT spectra, we introduce a scaling factor $\mathcal{B}_{\rm XUV}$, as a measure for the number of scattered electrons that are emitted per directly emitted (not scattered) photoelectron. We neglect contributions to $P_{\rm XUV}^{\rm bgr}$ from scattered ATI photoelectrons, since the IR pulse is reflected at $z_{\rm IR}$, close to the vacuum interface, and therefore does not release electrons in the bulk.

Addition of the background contributions to the direct photoelectron yield (1) results in the net photoelectron yield

$$P(\varepsilon_f, \tau) = P_0(\varepsilon_f, \tau) + P_{\rm XUV+IR}^{\rm bgr}(\varepsilon_f), \qquad (12)$$

with the background contribution

$$P_{\rm XUV+IR}^{\rm bgr}(\varepsilon_f) = \mathcal{B}_{\rm XUV} P_{\rm XUV}^{\rm bgr}(\varepsilon_f) + \mathcal{B}_{\rm IR} P_{\rm IR}^{\rm bgr}(\varepsilon_f). \qquad (13)$$

We note that the damping factor $f_{\varepsilon_f, \theta_f}$ in the final photoelectron state (5) and our modeling of the secondary electron yield include different aspects of the photoelectron propagation inside the solid. $f_{\varepsilon_f, \theta_f}$ models *emission-probability losses* due to collisions inside the substrate, i.e., this factor eliminates electrons that cannot reach the detector due to being excited more than a few mean free paths inside the substrate. The remaining emitted electrons generate the energy-dependent secondary electron yield $\mathcal{B}_{\rm XUV} P_{\rm XUV}^{\rm bgr}$.

III. NUMERICAL RESULTS

A. XUV photoemission spectra

In order to start to constrain the parameters of our model, we calculated XUV-photoionization spectra by monochromatic p-polarized pulses with photon energies between 20 and 60 eV (without assisting IR pulses). We selected an incidence angle of $45°$ and photoelectron emission perpendicular to the surface, in order to be able to compare our results with recently measured energy-resolved spectra obtained by Roth *et al.* [28]. This comparison allows us to adjust the parameters n, α, and U_0 in the initial- and final-state wave functions, separately for the
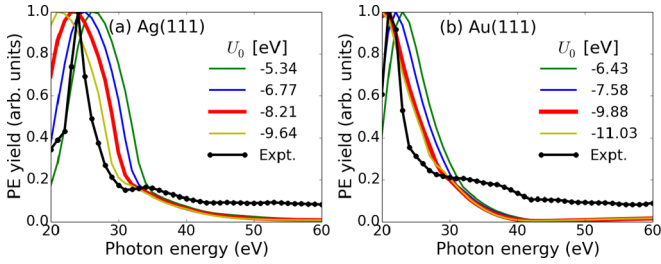
FIG. 3. Energy-resolved XUV photoelectron yield for (a) Ag(111) and (b) Au(111). Integrated yields $P_{\mathrm{XUV}}(\varepsilon_f)$ for different potential-step parameters U_0 in the final photoelectron wave function. Experimental yields are adapted from Roth *et al.* [28].

FIG. 4. Normalized background of secondary electrons $P_{\mathrm{XUV}}^{\mathrm{bgr}}$, above-threshold IR-pulse-ionization electrons $P_{\mathrm{IR}}^{\mathrm{bgr}}$, and interferometric electron yield P_0 without background contributions for (a) Ag(111) and (b) Au(111).

Ag(111) and Au(111) surface for different photon energies. The spectra recorded by Roth *et al.* used monochromatic synchrotron radiation with photon energies ranging from 20 to 120 eV. For photon energies ω between 20 and 60 eV we ε_f integrated $P_{\mathrm{XUV}}(\varepsilon_f)$ over an 1 eV interval centered at $\varepsilon_f^0 = E_{\mathrm{bnd}} + \omega$. The considered photon-energy range from 20 to 60 eV is sufficient, since it encompasses the APT spectral profile in the RABBITT experiment of Locher *et al.* [15].

Figure 3 shows the best fits of our integrated XUV photoemission yields as functions of the photon energy to the yields measured by Roth *et al.* [28]. They were obtained for the parameters $U_0 = -8.21$ eV, $n_H = 6$, and $\alpha_H = 0.38\ a_s^{\mathrm{Ag}}$ for the Ag surface and for $U_0 = -9.88$ eV, $n_H = 7$, and $\alpha_H = 0.35\ a_s^{\mathrm{Au}}$ for the Au surface. The above parameter values provided yield distributions centered at the experimental peaks. We searched for optimal parameters by comparing delay-integrated calculated yields with the experimental photoelectron yields, starting with a coarse parameter grid, subsequently exploring favorable parameter configurations on a finer grid. Our search strategy is based on the following parameter hierarchy and parameter ranges: (i) We limited the potential step U_0 to the upper and lower bounds of Chulkov potentials [23,31] inside the substrate for each material. (ii) We varied α_H between zero and half a lattice spacing, to keep the atomic-orbital nodes localized near the lattice points. (iii) Guided by the small number (1 and 2) of wave-function nodes of hydrogenic 4d and 5d orbitals, we model the d bands of Ag and Au by keeping the number of nodes n_H of the GSFs φ as small as possible, without entailing unphysical values for other parameters and while still matching the experimental peak localization. We used these substrate parameters for all time-resolved calculations discussed in the following sections.

B. RABBITT spectra and background contributions

As is obvious from the comparison of Figs. 2 and 4, the spectral distribution of the XUV pulse train HH amplitudes determines the overall energy-dependent structure of RABBITT spectra. Knowledge of the experimental APT spectrum eliminates the HH-component amplitudes from the list of adjustable parameters. Since the spectral phases of the APT used by Locher *et al.* [15] are not known and will be eliminated by subtracting the phases of the reference gas target, we calculated RABBITT spectra by (randomly) setting all spectral phases equal to zero.
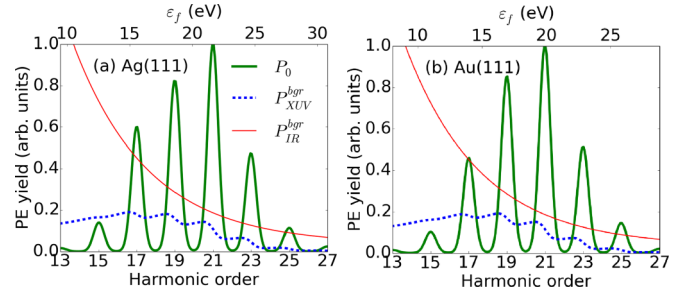
Figure 5 shows our calculated interferometric spectra for Ag(111) and Au(111) next to the experimental spectra. To achieve the best overall agreement with the measured Ag(111) spectrum, we multiplied the normalized secondary-electron background with $\mathcal{B}_{\mathrm{XUV}} = 32.5 \pm 10$ and the normalized IR contribution with $\mathcal{B}_{\mathrm{IR}} = 0.95 \pm 0.15$ [see Eq. (13)]. In the same way we determined $\mathcal{B}_{\mathrm{XUV}} = 24.5 \pm 15$ and $\mathcal{B}_{\mathrm{IR}} = 0.15 \pm 0.15$ for the Au(111) spectrum. Delay-integrated photoelectron yields $P(\varepsilon_f, \tau)$ [Eq. (12)], calculated within the error margins of $\mathcal{B}_{\mathrm{IR}}$ and $\mathcal{B}_{\mathrm{XUV}}$, are shown as the shaded areas in Fig. 6. Outside the error margins for $\mathcal{B}_{\mathrm{IR}}$ and $\mathcal{B}_{\mathrm{XUV}}$ our calculated delay-integrated spectra start to significantly deviate from the measured spectra. The significantly lower background contamination for the Au(111) spectrum is consistent with the larger work function of Au, 5.31 eV, as opposed to 4.74 eV for Ag(111) [45]. It is also in agreement with the data analysis in Ref. [15]. The screening parameter, introduced for the simulation of the secondary electron background in Eq. (10), leads to the best reproduction of the measured spectra if adjusted to $\alpha_Y = 0.5$ for the Ag and Au surfaces. α_Y screens
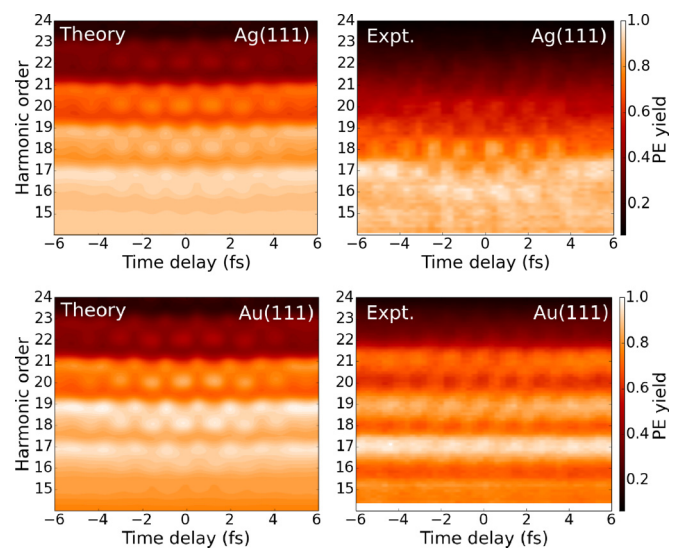

FIG. 5. RABBITT spectra for Ag(111) and Au(111). Spectra calculated according to Eq. (12), including secondary electron and above-threshold-ionization background (left). Experimental spectra adapted from Ref. [15] (right).
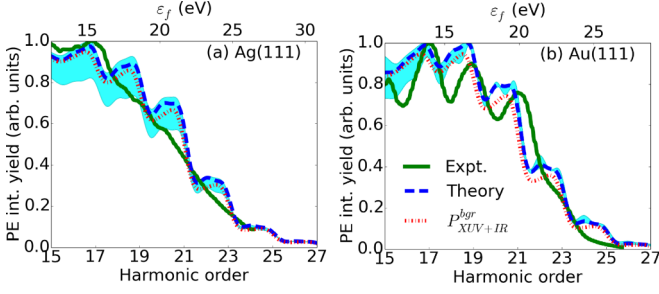
FIG. 6. Delay-integrated RABBITT spectra for Ag and Au obtained by integration of the spectra in Fig. 5 from −6 to 6 fs. Experimental spectra adapted from Ref. [15] (green solid line). Calculated spectra (blue dashed line) and secondary-electron background P_{XUV+IR}^{bgr} according to Eq. (11) (red dotted line). The cyan or gray shaded areas show the variation of the calculated electron yields within the uncertainty intervals for $\mathcal{B}_{XUV}$ and $\mathcal{B}_{IR}$.
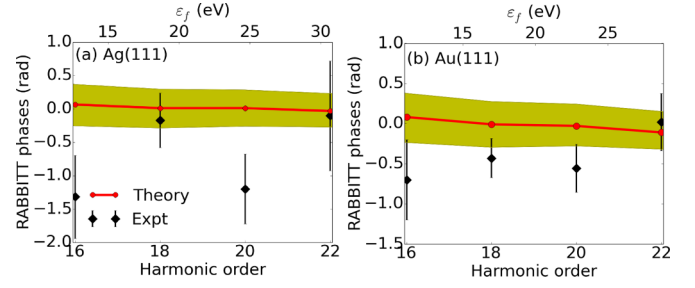

FIG. 7. RABBITT phases deduced from the interferometric photoemission yields in Fig. 5. Experimental phases adapted from Ref. [15] (black markers with error bars). Phases calculated for z_{IR} ranging from $-2a_s$ to $0.5a_s$ (yellow or grey band) and for $z_{IR} = -0.75a_s$ (red dots). Interpolation lines are added only to guide the eye.

the electronic repulsion, and its adjusted value is comparable with the Thomas-Fermi screening length for metals of ≈1 a.u. [42].

Integration of the RABBITT spectra in Fig. 5 over the delay range from −6.0 to 6.0 fs results in distinctly different energy-dependent spectra. The delay-integrated Ag(111) spectrum is characterized by an overall linear decrease of the yield with increasing photoelectron energy between HH orders 17 and 23. While the calculated spectrum reveals the spectral amplitude oscillation of the ATP, these oscillations are absent in the integrated measured spectrum [Fig. 6(a)]. In contrast, the integrated Au(111) spectrum in Fig. 6(b) shows an overall moderately declining yield between HH orders 17 and 21 that changes to a more rapid decrease above HH order 21, and the measured Au(111) spectrum clearly indicates the HH energies of the APT. Within the present model, the detailed energy dependence of the photoelectron yield depends on the z-dependent factors, $\phi_{k_{i,z}}$ and $\psi_{k_{f,z}}(z)$, of the initial- and final-state wave functions, respectively. The parameters in these factors are tuned to the XUV (-pulse-only) photoemission spectra of Ref. [28]. Keeping this subset of adjustable parameters in our simulation of RABBITT spectra, our trained model provides fair agreement with the measured integrated RABBITT yields in Fig. 6.

C. RABBITT phases

In general, sideband-yield oscillations in RABBITT spectra oscillate with twice the IR-pulse frequency and are phase-shifted relative to each other and relative to the carrier electric field of the assisting IR pulse [25]. We determined the RABBITT phases in our calculated spectra by integrating the photoemission yield $P(\varepsilon_f, \tau)$ over ε_f over a 0.6 eV energy interval centered at the central sideband energy. This results in integrated sideband yields $P_{2n}(\tau)$ for any given sideband order $2n$ which we mapped onto the expression

$$P_{2n}(\tau) = \left[a_1 \cos\left(2\omega_{IR}\tau - \phi_{2n}^{RAB}\right) + a_2\right] e^{-\left[\frac{(\tau - a_3)}{a_4}\right]^2} + a_5$$

by adjusting ϕ_{2n}^{RAB} and the parameters $a_{1,...,5}$.

The resulting RABBITT phases are shown in Fig. 7 for Ag(111) and Au(111) in comparison with the phases extracted

by Locher *et al.* [15] from their measured spectra. In order to assess the sensitivity of RABBITT phases to the photoelectron transport time in the solid, we varied the onset of the IR field z_{IR} from z_{im} to $-2.0a_s$. Our calculated RABBITT phases vary within the yellow (grey) band. Larger values of z_{IR} correspond to larger phases. We adopted $z_{IR} = -0.75a_s$, which is compatible with the range of IR skin depths deduced in Ref. [14], as the physically most reasonable value. It results in the phases shown as red markers connected by the red line.

Our calculations predict a similar baseline level for the RABBITT phases

$$\phi_{2n}^{RAB} = 2\phi^{Fres} + \phi_{prop} + \phi_{sc,2n}^{RAB} \tag{14}$$

for Ag(111) and Au(111) (Fig. 7). These include a dominant contribution $2\phi^{Fres}$ that is due to the Fresnel reflection of the IR pulse [23]. This phase contribution amounts to $2\phi^{Fres} = -1.52$ rad for Ag and -1.60 rad for Au. We added to our theoretical phases shown Fig. 7 the experimental beam propagation phase $\phi_{prop} = 0.643$ rad, which is accumulated during the pulse propagation from the reference argon gas cell to the surface under scrutiny (see supplementary material in [15]).

The experimental phases ϕ_{2n}^{RAB} for Ag(111) in Fig. 7(a) exhibit large fluctuations from one harmonic order to the next that our model does not reproduce. The measured RABBITT phases for Au(111) [Fig. 7(b)], in contrast, oscillate with a much smaller amplitude and thus deviate much less from the ballistic transport regime. Our calculated RABBITT phases show a similar smooth and slowly varying behavior as a function of photoelectron energy as the theoretical phases, obtained within a ballistic transport model, in Fig. 5 of Ref. [15]. The deviation from the experimental phases suggests that for the considered photon energies the assumption of classical photoelectron transport in and near the substrate may not be valid, as is also conjectured in Ref. [19]. This conjuncture is also consistent with the observation in Ref. [17] that up to ≈30 eV the dispersion of photoelectrons is determined by the substrate and strongly differs from free-electron propagation. This suggests a refined modeling of the final state with more emphasis on details of substrate electronic structure, which is outside the scope of the present study.

IV. SUMMARY

We calculated interferometric photoemission spectra from the (111) surfaces of Au and Ag, including background contributions from secondary electrons and direct emission by the IR pulse. Our simulation includes parameters that we adjusted (i) to energy-resolved XUV photoelectron spectra recently measured at a synchrotron light source by Roth *et al.* [28] and (ii) to obtain the best overall agreement with interferometric spectra measured by Locher *et al.* [15]. Our model is based on the evaluation of the quantum-mechanical transition amplitude in the nondipole velocity gauge between translationally invariant initial conduction-band states and final photoelectron states that include the photoelectron interaction with the inhomogeneous electric field of the Fresnel-reflected IR pulse, propagation of the photoexcited electron inside the solid, and the effect of the potential increase at the solid surface.

Based on our quantum-mechanical model and adjusted parameters, we observe dominant contributions to the photoelectron yield from secondary electrons. We find smaller background contributions from the Au(111) than from the Ag(111) surface, in qualitative agreement with Au having a larger work function than Ag. Including secondary-electron and above-threshold-ionization background contributions, our simulations are in fair agreement with the experimental RABBITT spectra from Ag(111) and Au(111) surfaces of Ref. [15].

We find that all RABBITT phases are strongly affected by Fresnel reflection of the IR pulse. The significant differences of the measured Ag(111) RABBITT phases for different sideband orders remains to be explained. As our model includes the influence of the surface electronic structure on the *final* state of the photoelectron in a somewhat rudimentary way, assuming a sharp potential-energy decline at the surface and free-electron dispersion, its inability to reproduce the observed phase oscillation may be seen as evidence for relevant final-state photoelectron-surface interactions not included in our simulation. We intend to address this effect in a future publication.

[1] S. Hüfner, *Photoelectron Spectroscopy: Principles and Applications* (Springer, Berlin, 2003).

[2] S. R. Leone, C. W. McCurdy, J. Burgdörfer, L. S. Cederbaum, Z. Chang, N. Dudovich, J. Feist, C. H. Greene, M. Ivanov, R. Kienberger, U. Keller, M. F. Kling, Z.-H. Loh, T. Pfeifer, A. N. Pfeiffer, R. Santra, K. Schafer, A. Stolow, U. Thumm, and M. J. J. Vrakking, Nat. Photon. **8**, 162 (2014).

[3] U. Thumm, Q. Liao, E. M. Bothschafter, F. Süßmann, M. F. Kling, and R. Kienberger, in *The Oxford Handbook of Innovation*, edited by D. Andrew (Wiley, New York, 2015), Chap. 13.

[4] F. Calegari, G. Sansone, S. Stagira, C. Vozzi, and M. Nisoli, J. Phys. B **49**, 062001 (2016).

[5] M. Hentschel, R. Kienberger, C. Spielmann, G. A. Reider, N. Milosevic, T. Brabec, P. Corkum, U. Heinzmann, M. Drescher, and F. Krausz, Nature **414**, 509 (2001).

[6] M. Schultze, M. Fieß, N. Karpowicz, J. Gagnon, M. Korbman, M. Hofstetter, S. Neppl, A. L. Cavalieri, Y. Komninos, T. Mercouris, C. A. Nicolaides, R. Pazourek, S. Nagele, J. Feist, J. Burgdörfer, A. M. Azzeer, R. Ernstorfer, R. Kienberger, U. Kleineberg, E. Goulielmakis, F. Krausz, and V. S. Yakovlev, Science **328**, 1658 (2010).

[7] K. Klünder, J. M. Dahlström, M. Gisselbrecht, T. Fordell, M. Swoboda, D. Guénot, P. Johnsson, J. Caillat, J. Mauritsson, A. Maquet, R. Taïeb, and A. L'Huillier, Phys. Rev. Lett. **106**, 143002 (2011).

[8] C. Palatchi, J. M. Dahlström, A. S. Kheifets, I. A. Ivanov, D. M. Canaday, P. Agostini, and L. F. DiMauro, J. Phys. B **47**, 245003 (2014).

[9] S. Heuser, A. Jiménez Galán, C. Cirelli, C. Marante, M. Sabbar, R. Boge, M. Lucchini, L. Gallmann, I. Ivanov, A. S. Kheifets, J. M. Dahlström, E. Lindroth, L. Argenti, F. Martín, and U. Keller, Phys. Rev. A **94**, 063409 (2016).

[10] M. Ossiander, F. Siegrist, V. Shirvanyan, R. Pazourek, A. Sommer, T. Latka, A. Guggenmos, S. Nagele, J. Feist, J. Burgdörfer, R. Kienberger, and M. Schultze, Nat. Phys. **13**, 280 (2017).

[11] M. Huppert, I. Jordan, D. Baykusheva, A. von Conta, and H. J. Wörner, Phys. Rev. Lett. **117**, 093001 (2016).

[12] A. L. Cavalieri, N. Muller, T. Uphues, V. S. Yakovlev, A. Baltuska, B. Horvath, B. Schmidt, L. Blumel, R. Holzwarth, S. Hendel, M. Drescher, U. Kleineberg, P. M. Echenique, R. Kienberger, F. Krausz, and U. Heinzmann, Nature **449**, 1029 (2007).

[13] S. Neppl, R. Ernstorfer, E. M. Bothschafter, A. L. Cavalieri, D. Menzel, J. V. Barth, F. Krausz, R. Kienberger, and P. Feulner, Phys. Rev. Lett. **109**, 087401 (2012).

[14] S. Neppl, R. Ernstorfer, A. L. Cavalieri, C. Lemell, G. Wachter, E. Magerl, E. M. Bothschafter, M. Jobst, M. Hofstetter, U. Kleineberg, J. V. Barth, D. Menzel, J. Burgdörfer, P. Feulner, F. Krausz, and R. Kienberger, Nature **517**, 342 (2015).

[15] R. Locher, L. Castiglioni, M. Lucchini, M. Greif, L. Gallmann, J. Osterwalder, M. Hengsberger, and U. Keller, Optica **2**, 405 (2015).

[16] M. Lucchini, L. Castiglioni, L. Kasmi, P. Kliuiev, A. Ludwig, M. Greif, J. Osterwalder, M. Hengsberger, L. Gallmann, and U. Keller, Phys. Rev. Lett. **115**, 137401 (2015).

[17] Z. Tao, C. Chen, T. Szilvási, M. Keller, M. Mavrikakis, H. Kapteyn, and M. Murnane, Science **353**, 62 (2016).

[18] C. Chen, Z. Tao, A. Carr, P. Matyba, T. Szilvási, S. Emmerich, M. Piecuch, M. Keller, D. Zusin, S. Eich, M. Rollinger, W. You, S. Mathias, U. Thumm, M. Mavrikakis, M. Aeschlimann, P. M.

Oppeneer, H. Kapteyn, and M. Murnane, Proc. Natl. Acad. Sci. USA **114**, E5300 (2017).

[19] L. Kasmi, M. Lucchini, L. Castiglioni, P. Kliuiev, J. Osterwalder, M. Hengsberger, L. Gallmann, P. Krüger, and U. Keller, Optica **4**, 1492 (2017).

[20] F. Siek, S. Neb, P. Bartz, M. Hensen, C. Strüber, S. Fiechter, M. Torrent-Sucarrat, V. M. Silkin, E. E. Krasovskii, N. M. Kabachnik, S. Fritzsche, R. D. Muiño, P. M. Echenique, A. K. Kazansky, N. Müller, W. Pfeiffer, and U. Heinzmann, Science **357**, 1274 (2017).

[21] P. M. Paul, E. S. Toma, P. Breger, G. Mullot, F. Augé, P. Balcou, H. G. Muller, and P. Agostini, Science **292**, 1689 (2001).

[22] J. Mauritsson, M. B. Gaarde, and K. J. Schafer, Phys. Rev. A **72**, 013401 (2005).

[23] M. J. Ambrosio and U. Thumm, Phys. Rev. A **94**, 063424 (2016).

[24] M. Lucchini, A. Ludwig, L. Kasmi, L. Gallmann, and U. Keller, Opt. Express **23**, 8867 (2015).

[25] M. J. Ambrosio and U. Thumm, Phys. Rev. A **96**, 051403 (2017).

[26] Q. Liao and U. Thumm, Phys. Rev. Lett. **112**, 023602 (2014).

[27] Q. Liao and U. Thumm, Phys. Rev. A **89**, 033849 (2014).

[28] F. Roth, T. Arion, H. Kaser, A. Gottwald, and W. Eberhardt, J. Electron Spectrosc. **224**, 84 (2018).

[29] L. Castiglioni (private communication).

[30] S. Tanuma, C. J. Powell, and D. R. Penn, Surf. Interface Anal. **43**, 689 (2011).

[31] E. Chulkov, V. Silkin, and P. Echenique, Surf. Sci. **437**, 330 (1999).

[32] E. Palik, *Handbook of Optical Constants in Solids* (Academic, San Diego, 1998).

[33] M. J. Ambrosio, J. A. Del Punta, K. V. Rodriguez, G. Gasaneo, and L. U. Ancarani, J. Phys. A **45**, 015201 (2012).

[34] A. L. Frapiccini, G. Gasaneo, F. Colavecchia, and D. Mitnik, J. Electron Spectrosc. **161**, 199 (2007).

[35] M. J. Ambrosio, D. M. Mitnik, L. U. Ancarani, G. Gasaneo, and E. L. Gaggioli, Phys. Rev. A **92**, 042704 (2015).

[36] P. S. Wehner, R. S. Williams, S. D. Kevan, D. Denley, and D. A. Shirley, Phys. Rev. B **19**, 6164 (1979).

[37] K. A. Mills, R. F. Davis, S. D. Kevan, G. Thornton, and D. A. Shirley, Phys. Rev. B **22**, 581 (1980).

[38] D. M. Volkov, Z. Phys. **94**, 250 (1935).

[39] W. Greiner, *Classical Electromagnetism* (Springer, New York, 1996).

[40] A. D. Rakić, A. B. Djurišić, J. M. Elazar, and M. L. Majewski, Appl. Opt. **37**, 5271 (1998).

[41] P. B. Johnson and R. W. Christy, Phys. Rev. B **6**, 4370 (1972).

[42] N. W. Ashcroft and N. D. Mermin, *Solid State Physics* (Harcourt College Publishers, Orlando, 1976).

[43] C. Cohen-Tannoudji, B. Diu, and F. Laloë, *Quantum Mechanics* (Wiley, New York, 1977), Vol. 2.

[44] C. J. Joachain, *Quantum Collision Theory* (North Holland, New York, 1975).

[45] H. L. Skriver and N. M. Rosengaard, Phys. Rev. B **46**, 7157 (1992).